Biophysical Journal, Volume *116*

Supplemental Information

Decoding Calcium Signaling Dynamics during *Drosophila* Wing Disc Development

Pavel A. Brodskiy, Qinfeng Wu, Dharsan K. Soundarrajan, Francisco J. Huizar, Jianxu Chen, Peixian Liang, Cody Narciso, Megan K. Levis, Ninfamaria Arredondo-Walsh, Danny Z. Chen, and Jeremiah J. Zartman

Supplemental information for:
Decoding calcium signaling dynamics during *Drosophila* wing disc development

Pavel A. Brodskiy[1,†], Qinfeng Wu[1,†], Dharsan K. Soundarrajan[1], Francisco J. Huizar[1], Jianxu Chen[2], Peixian Liang[2], Cody Narciso[1], Megan K. Levis[1], Ninfamaria Arredondo-Walsh[1], Danny Z. Chen[2], and Jeremiah J. Zartman[1,*]

[1] Department of Chemical and Biomolecular Engineering, University of Notre Dame, Notre Dame, Indiana, 46556, USA
[2] Department of Computer Science and Engineering, University of Notre Dame, Notre Dame, Indiana, 46556, USA

[†] These authors contributed equally to this work
[*] Corresponding author

Supplemental material and methods

Fly strains and genetics

Unless otherwise indicated, stocks were obtained from Bloomington *Drosophila* Stock Center as indicated by stock number (BL#). Progeny wing phenotypes are from F1 male progeny emerging from the nub-Gal4, UAS-GCaMP6f/CyO x UAS-X cross. Representative results are summarized in Table S3. Male progenies were selected to avoid variation in wing size due to sex. The tester line (w1118; nubbin-GAL4, UAS-GCaMP6f/CyO) was generated as previously described (29). Flies were raised at 25 °C and 12-hour light cycle. When possible, we also performed multiple RNAi tests and selected the most severe phenotype for additional analysis. For perturbations to morphogenetic signaling, RNAi line phenotypes were consistent with loss-of-function phenotypes for target genes (Figure S7).

Fly extract preparation

One-gram well-nourished mature flies were homogenized in a tissue homogenizer (15 ml capacity, 0-1 mm clearance) with 6.82 ml of ZB media. Some fly extract was also ordered from Drosophila Genomics Resource Center. This homogenate was centrifuged at 2600 rpm for 20 min at 4°C. The supernatant and the oily film above it were removed and heat-treated at 60°C for 20 min. This preparation was then spun at 2600 rpm for 90 min at 4°C. The supernatant (fly extract) was removed, sterilized by 0.2 µm filtration, and stored at 4°C.

Wing disc imaging setup

We used two methods to culture the wing disc for imaging:

Culture method 1 is a modification of the procedure described in (42): We truncated the legs of a cell culture insert (EDM Millipore).” We then put the insert on top of a pool of pool of media to immobilize the wing discs. 50 µL of embryo oil was added along the outer periphery of the insert to seal. 100 µL of organ culture media was added on top of membrane of the insert (42).

Culture method 2 is described in (29), which reduced organ motion compared to method 1.

Imaging was performed on a Nikon Eclipse T*i* confocal microscope (Nikon Instruments, Melville, NY) with a Yokogawa spinning disc and MicroPoint laser ablation system (Andor Technology, South Windsor, CT). Image data were collected on an iXonEM+ cooled CCD camera (Andor Technology, South Windsor, CT) using MetaMorph® v7.7.9 software (Molecular Devices, Sunnyvale, CA). We found that the GCaMP6f sensor saturated at 80% laser intensity, but that intensity was linearly related at values under 70% (Fig. S5). Image intensity was linearly normalized to be comparable at 50% laser intensity.

Identification of the axes

Each image was presented as a 2x2 grid of the image either not transformed, flipped left/right, flipped top/down, or rotated 180 degrees in random order. The user selected the correctly-oriented pouch. The order in which the pouches were displayed was randomized, and a consensus was reached once three guesses were made if all three were the same. 77% of the samples were unambiguously classified in the first attempt in this way. If the first three guesses were not the same, then when more than half of the guesses were the same orientation, the most common orientation was taken to be the consensus. Two images were removed from the analysis because no consensus was reached after seven attempts.

Feature extraction

Each signal was decomposed into the following features: amplitude, frequency and integrated intensity, which comprise the Ca^{2+} signature of the ROI. Amplitude is defined as the mean of the amplitudes of the peaks, where the amplitude of each peak is the prominence of the peak in the *findpeaks* algorithm. F (mHz) is the number of peaks detected divided by the length of the signal in time (Fig. 6C, Fig. S1D-E). The integrated intensity (a.u.) is the time-averaged integral of the signal over time using a trapezoidal approximation.

The normalized intensity ($\Delta I(t)/I_o$) was approximated by using a bandpass Gaussian filter, where the larger sigma value adjusted for change in basal level over time, and the smaller sigma value compensated for stochastic noise. Spikes in signaling activity were extracted from $\Delta I(t)/I_0$ using the MATLAB *findpeaks* algorithm, with a minimum amplitude (Amp_{min}) and refractory period. MATLAB's genetic algorithm *ga* was used to calibrate the feature extraction parameters (Fig. 6C, Fig. S3, Table S4). To generate reference values for optimization of feature extraction parameters, 233 signals (I(t)) were randomly selected from 656,000 total signals, and manually annotated to identify the times (t_1 and t_2) at which each peak begins and ends. From this, the basal level was taken to be:

$$B_{manual} = \min\big(I(t\epsilon[t_1, t_2])\big)$$

the amplitude was extracted, as equal to:

$$Amp_{manual} = \max\big(I(t\epsilon[t_1, t_2])\big) - B_{manual}$$

and the width at half max (WHM) was taken to be the total time that the signal was greater than the average of the amplitude:

$$\mathrm{WHM}_{manual} = \mathrm{sum}\left(I(t\epsilon[t_1, t_2]) > \frac{(Amp_{manual} - B_{manual})}{2}\right)$$

The genetic algorithm was run at default settings for 172 generations. The objective function Err_1 was the sum of the squared differences of the correlation coefficients of the manual measurements and automatic measurements normalized to manual measurements. Err_2 was the fraction of signals with no waves incorrectly selected to contain waves compared to the manual ground-truth annotated data:

$$Err_1 = \sqrt{\left(\frac{Amp_{manual} - Amp_{auto}}{Amp_{manual}}\right)^2 + \left(\frac{WHM_{manual} - WHM_{auto}}{WHM_{manual}}\right)^2 + \left(\frac{B_{manual} - B_{auto}}{B_{manual}}\right)^2}$$

$$Err_2 = \frac{1}{N}\sum_{i}^{N}(WHM_{manual} = 0 \,\&\, WHM_{auto} > 0)$$

where N is the number of signals analyzed (N = 233). A Pareto front was generated to demonstrate the trade-offs between summary statistic error and false positives. Parameter values were selected that minimized both measurement error and false positives (Fig. S3, Table S4).

Statistical analysis and visualization

To compare across compartments, medians were taken after dividing discs into A compartment and P compartment such that the A-P compartment boundary was approximated with a vertical line fitted to points along the A/P axis. A two-tailed, paired Student's t-test was performed. The F-test for model fit relative to a constant model was used to determine whether each summary statistic was related to pouch size. As outlined in Fig. 6, spatial maps were generated for each wing disc to explore the impact of spatial position, developmental progression, and genetic perturbations on Ca^{2+} signatures. The composite maps in Fig. 7 represent the consensus of multiple wing discs from each condition. These spatial composites were mapped to a canonical described in (52) (Fig. S4)

Qualitative analysis

Qualitative analysis was reported in Fig. 3F,G, 5E,F, and 7C. Each bar represents the overall fraction of time discs undergo each class of signaling. Each measurement indicates a class assigned to an individual video clip, and each measurement was weighted equally. nub-GCaMP6 serves as controls. nub-GCaMP6 represents measurements taken from wandering larvae. Results of proportions test for Fig. 5F and 7C are summarized in Table S6 and S7. Analysis for Fig. 3F,G, and 5E,F was performed using an ordinal regression to determine whether pouch size significantly impacts the class of Ca^{2+} activity. This analysis assumes a hierarchy of activity with no activity being the least active category and "fluttering" being the most active category. This hierarchy activity is established based the FEX dose-response experiments in Fig. 3.

Experimental limitations

It can be noted that a possible limitation of the present study is the use of the GCaMP6f-based reporters to visualize Ca^{2+} signaling activity. For example, certain levels of Ca^{2+} might be out of the range of detection of the GCaMP6f sensor. It may be possible that a different Ca^{2+} sensor with a different affinity to Ca^{2+} may report different Ca^{2+} dynamics. Further, we cannot rule out the

possibility that genetic perturbations might impact total levels of GCaMP6f expression under the nub-Gal4 driver. This can be addressed in future studies by systematic ratiometric measurements of Ca^{2+} such as normalizing to mCherry expression and by comparing additional readouts of calcium signaling as new techniques are developed.

Index of Supplementary Figures:

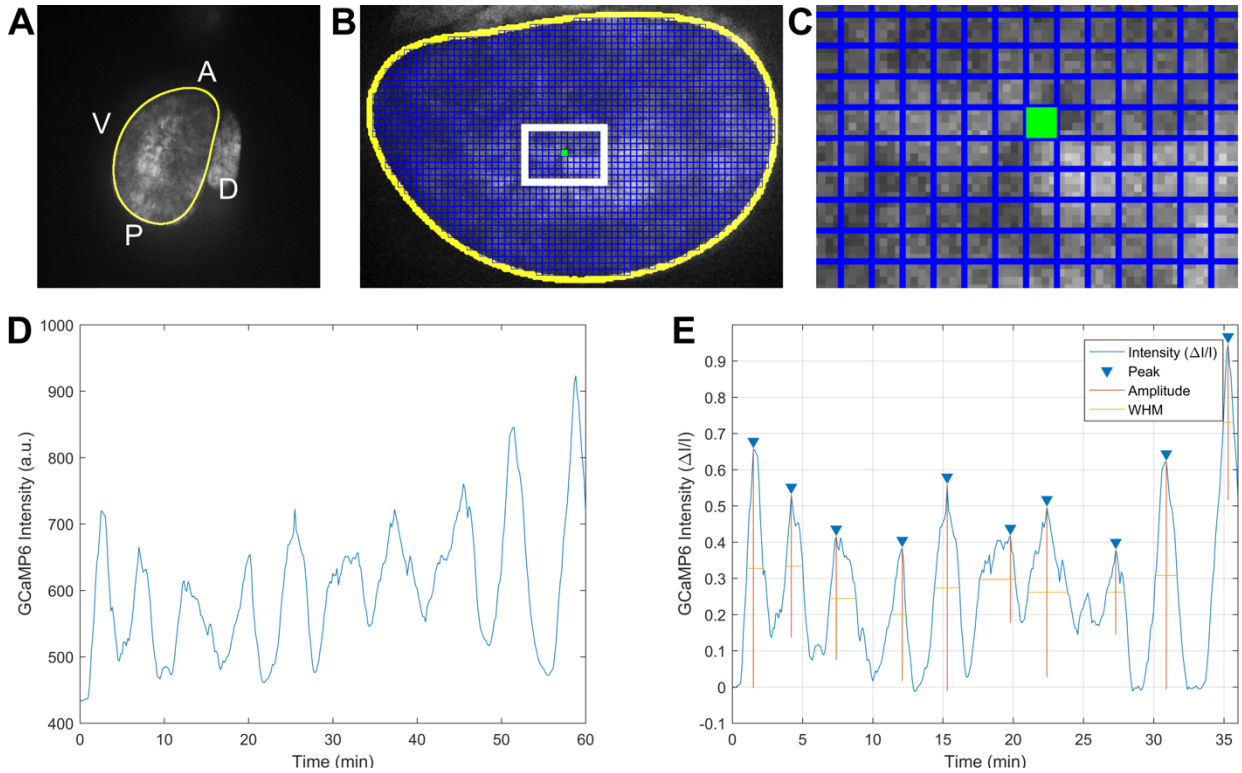

Figure S1: Signal extraction from wing discs

(A) Maximum intensity Z-projection of one frame of time-lapse video. (B) Manual mask around pouch, and grid of square regions of interest (ROIs). (C) Individual ROI is averaged over space to obtain a one-dimensional intensity profile. (D) Raw intensity profile. (E) Normalized intensity profile with amplitudes and widths at half max (WHM) marked.

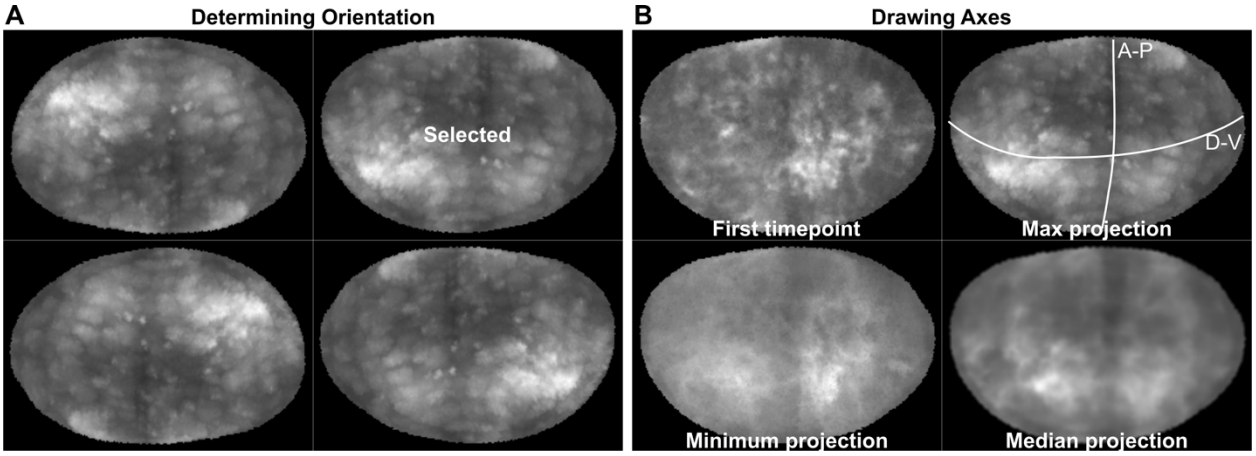

Figure S2: Manual identification of the wing disc pouch orientation

(A) Workflow for manual selection of orientation. Registered time stack was max projected over time in FIJI. The maximum projection was shown in a 2 x 2 format to the user with a non-processed, horizontally-flipped, vertically-flipped, and 180-degree rotated image presented in a random order. The user selected the image with the P compartment on the right and the D compartment on the top. Based on size and orientation, landmarks used to make the classification include the shape and size of the compartments as indicated in Fig. 1B. The pouches were presented in a random order and were repeated at least three times. If all three initial classifications were the same, that orientation was taken to be the consensus. If more than three attempts were needed, a consensus was reached when more than half of the selected discs were the same orientation. Two discs did not reach a consensus orientation after seven attempts and were not included in the analysis. (B) Workflow for axes selection. The first timepoint, max projection, min projection, and median projection were shown to the user in a 2x2 format. Curves were drawn for the A-P and D-V axes. The A-P axis generally aligns with a sharp decrease in intensity on the maximum projection, and the D-V axis generally aligns with an increase in basal level on the minimum projection. White lines indicate manual annotations of axes.

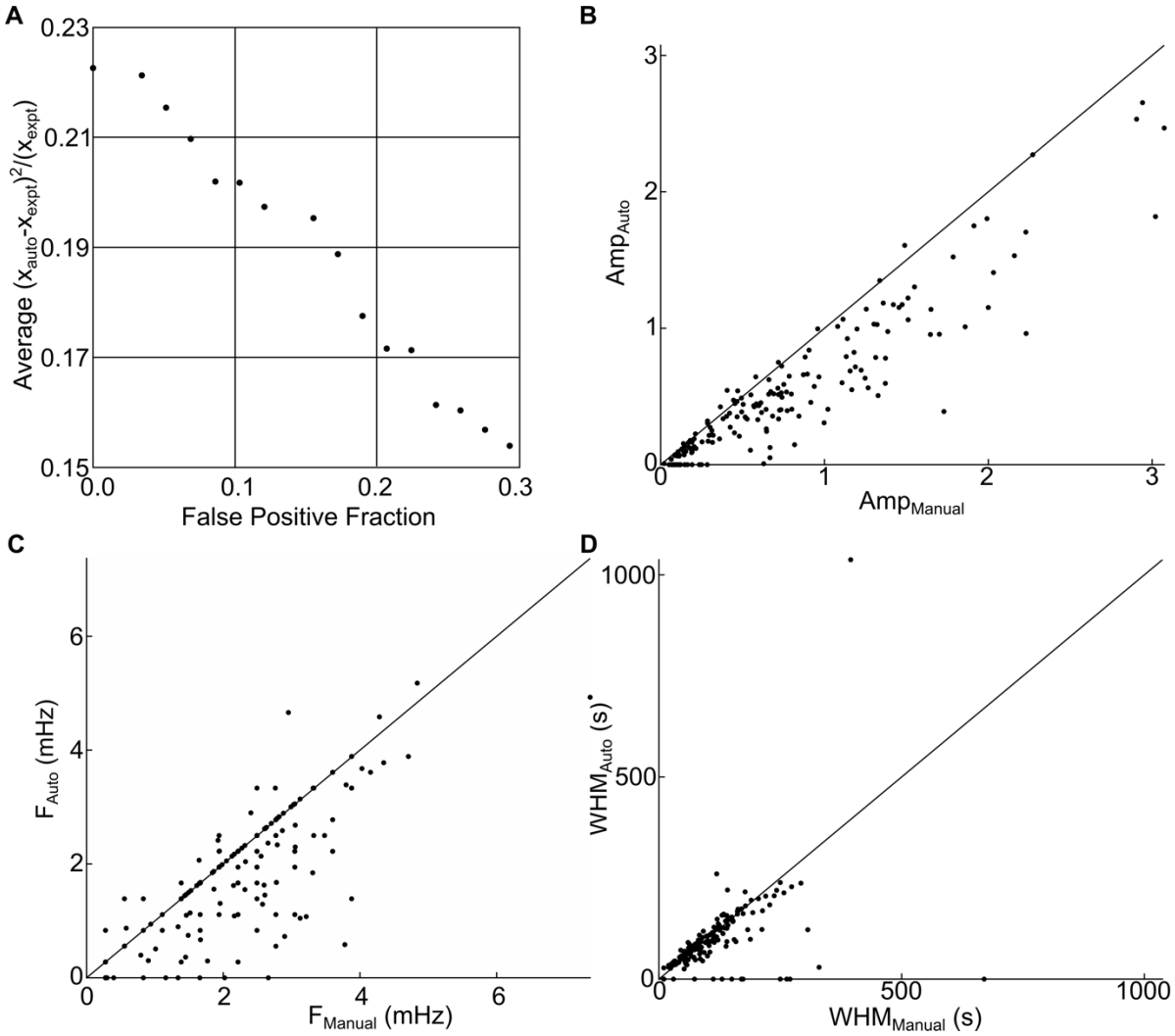

Figure S3: Optimization of image analysis parameters

(A) Pareto optimization chart for final solution. b-d, Comparison of automatically-extracted values and manually measured values for (B) frequency, (C) amplitude, and (D) time between peaks.

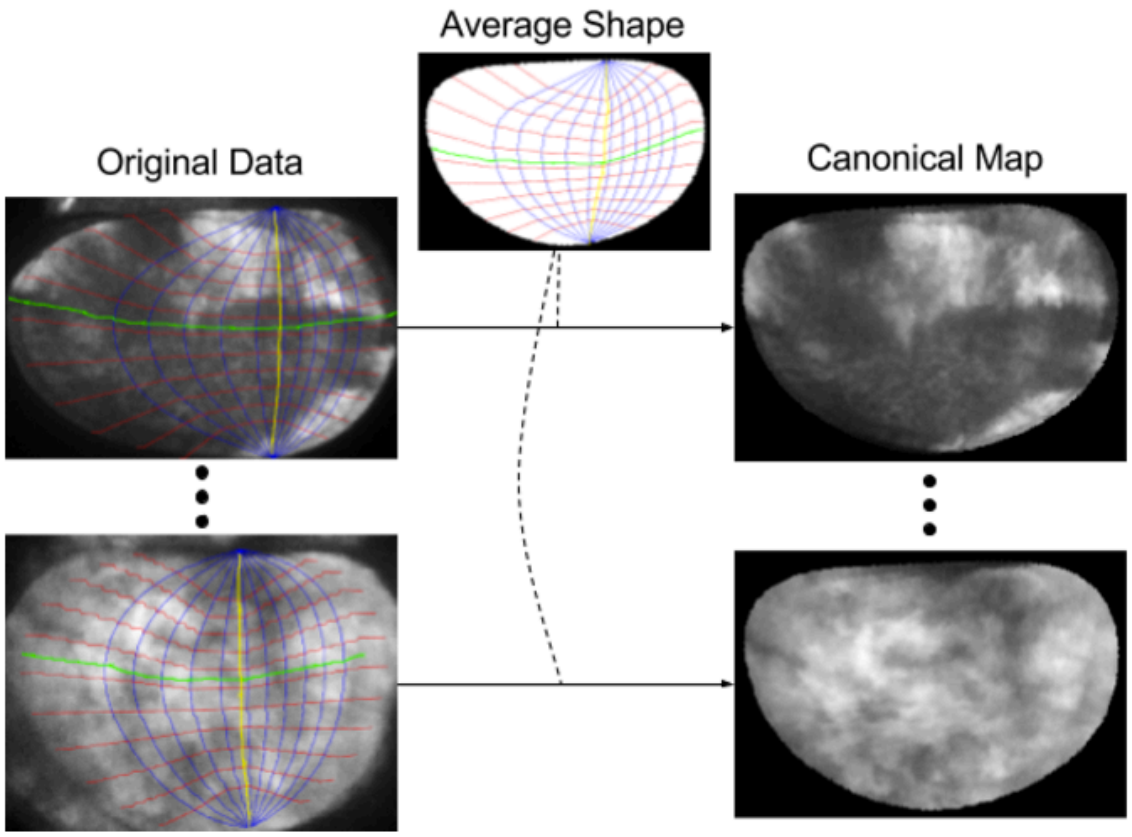

Figure S4: Transformation of spatial maps onto a canonical axis
A pouch coordinate system is defined along the A/P axis (the green curve) and the D/V axis (the yellow curve), similar to the latitude (cf. red curves) and longitude (cf. blue curves) of the geographic coordinate system. This coordinate system is constructed for each pouch. A mapping from the pouch coordinates in an input image to the corresponding pouch coordinates of the average shape transforms the original data to a canonical map.

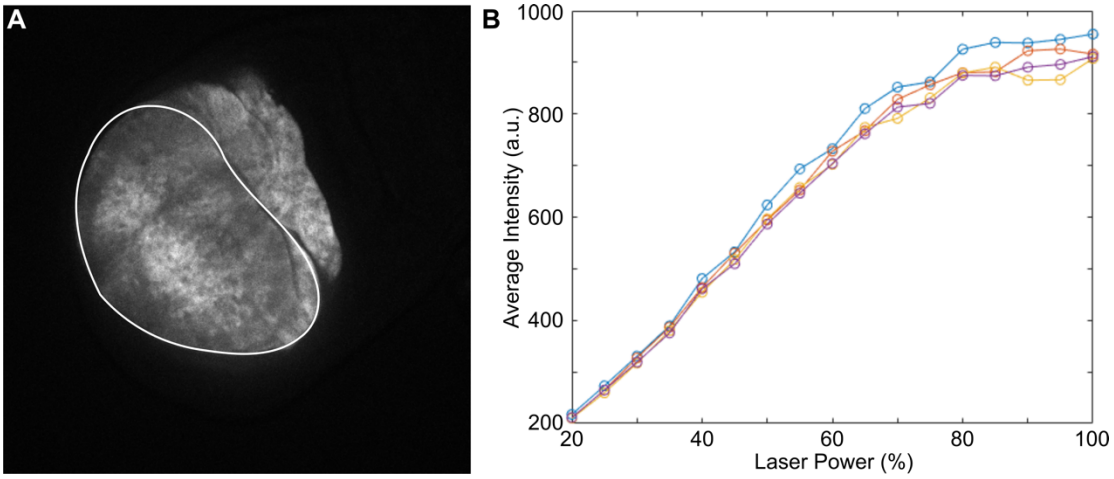

Figure S5: Correlation of laser power with image intensity

(A) Z-projection of confocal image of nub-GCaMP6f wing disc acquired at a laser power of 50% (n = 4). Pouch was segmented, and the average intensity of the pouch was obtained at various laser powers. (B) Average intensity of the pouch varies linearly with laser intensity under 80%.

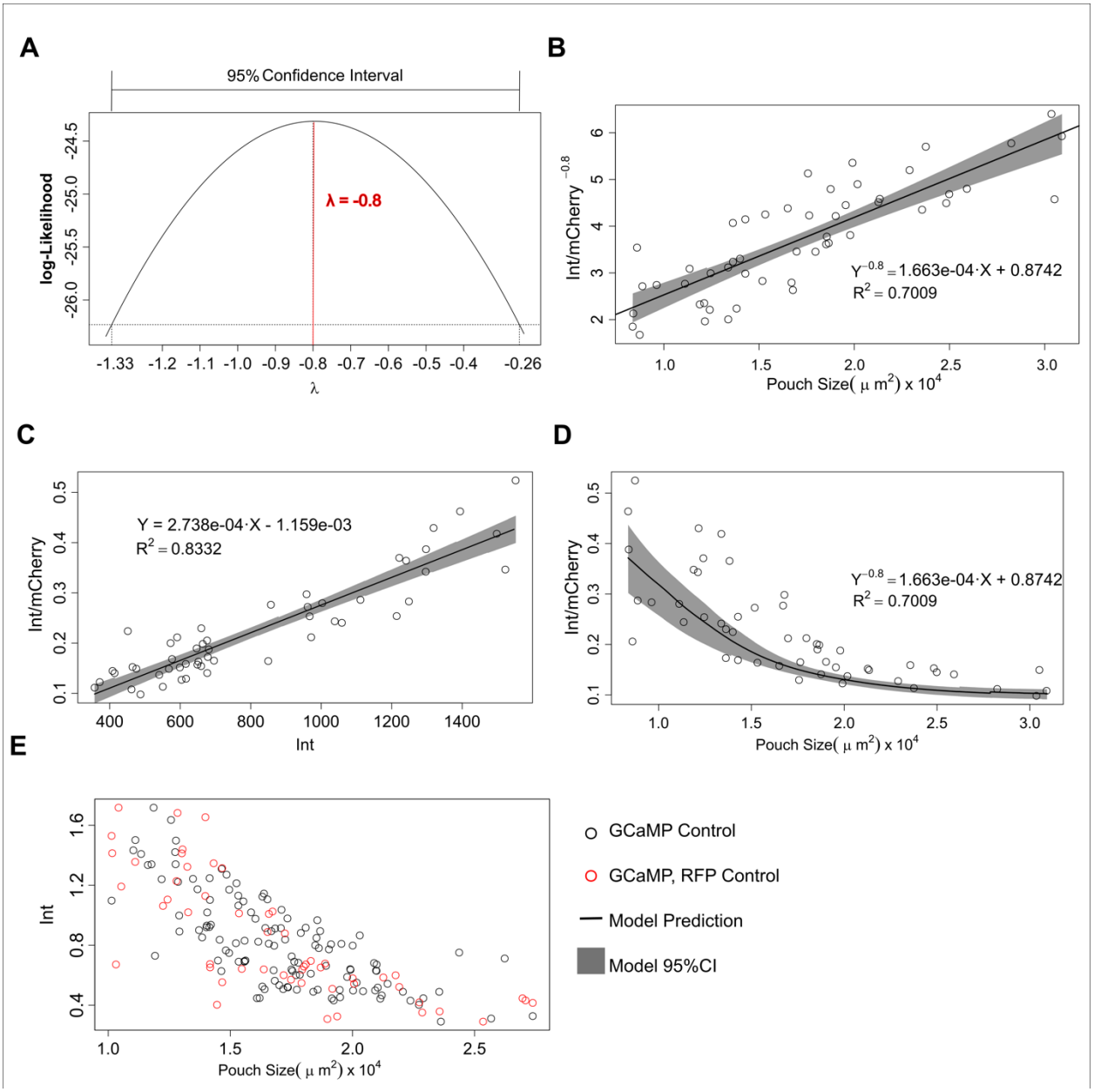

Figure S6: Normalized and unnormalized integrated intensities are highly correlated

A) Log-likelihood estimation of a parameter lambda to be used as an exponent in a power transformation of the data set. The maximum likelihood estimate of lambda was found to be -0.8 ± 0.53. This falls within the range of quarter-power scaling that has observed to occur in many biological contexts. B) Integrated intensity normalized to mCherry intensity is correlated to pouch size in a -0.80-power scaling fashion (R^2 = 0.70). Linear fit of power-transformed intensity from the log-likelihood estimation of λ. C) Normalized integrated intensity is correlated to unnormalized integrated intensity with a linear fit (R^2 = 0.83). D) Integrated intensity normalized to mCherry intensity with the back-transformed fit. E) Unnormalized integrated intensity for both nub-Gal4>UAS-GCaMP6f and nub-Gal4>UAS-GCaMP6f/ >UAS-mCherry. Justification of the power-scaling model is addressed in Fig. S7. CI: confidence interval.

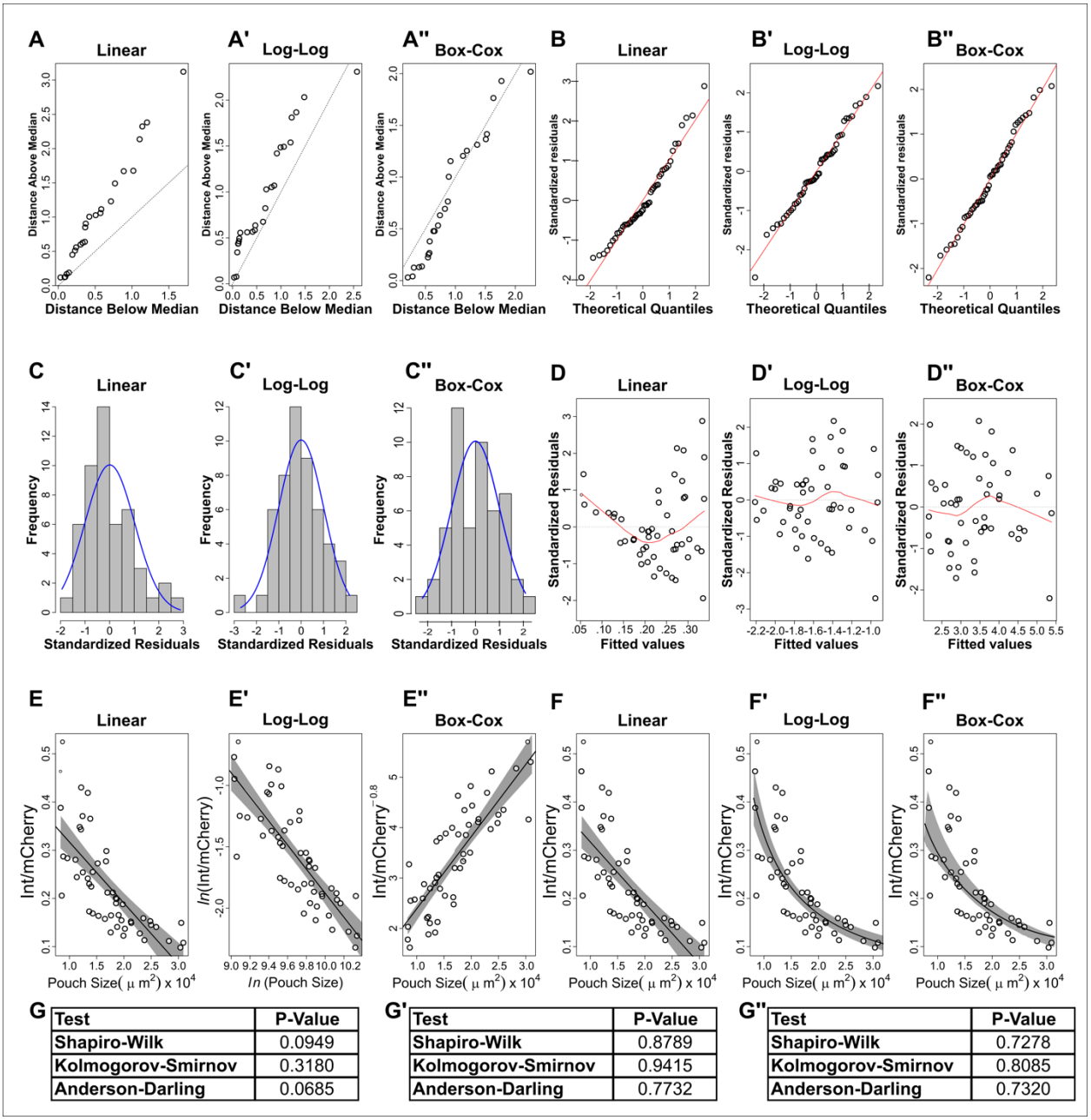

G

Test	P-Value
Shapiro-Wilk	0.0949
Kolmogorov-Smirnov	0.3180
Anderson-Darling	0.0685

G'

Test	P-Value
Shapiro-Wilk	0.8789
Kolmogorov-Smirnov	0.9415
Anderson-Darling	0.7732

G"

Test	P-Value
Shapiro-Wilk	0.7278
Kolmogorov-Smirnov	0.8085
Anderson-Darling	0.7320

Figure S7: Evaluation of linear, exponential, and power models for ratiometric (normalized) integrated intensity vs. pouch size

Comparison of regression models. A) Symmetry distributions of standardized residuals around the medians. Residuals are normally distributed if data on both sides of the median are equally distributed. Both linear and log-log transformed residuals show clear signs of asymmetry whereas the Box-Cox power-scaled transformation is evenly distributed around the median. B) Quantile-Quantile plots of the standardized residuals. If the residuals are from a normal distribution, they will lie on the red line that has an intercept equal to the mean of the residuals and a slope equal to the standard deviation. Linear model is heavily skewed while the log-log transformed model is slightly skewed to the left. Box-Cox power-scaled model has the best distribution along the red

line. C) Histograms of the standardized residuals with a blue superimposed normal curve. Residuals that are normally distributed should follow along the blue curve. The linear model residuals are heavily skewed while the log-log and power-scaled models have roughly normal distributions. D) Residuals versus fitted values of the standardized residuals. Residuals have constant variance if the values are centered around the dashed zero line. A red line is superimposed detailing the spread of the residuals. The linear model has non-constant variance in the residuals while the log-log model and power-scale model both have constant variance. E) Linear fits of each model to the untransformed data in the case of the linear model and the transformed data in the case of the log-log and power-scale model. The black line denotes the regression line and the surrounding grey bounds represent the 95% confidence interval of the regression line. F) Back-transformed fits of each model to untransformed data. G) Three normality tests were performed on the model residuals: Shapiro-Wilk, Kolmogorov-Smirnov, and Anderson-Darling. For the Shapiro-Wilk test, a p-value below 0.05 indicates there is evidence that the data tested are not from a normally distributed population. For the Kolmogorov-Smirnov normality test, a p-value closer to one provides evidence that the sample is drawn from a normal distribution. For the Anderson-Darling test, a p-value below 0.05 would indicate there is evidence that the data does not conform to a normal distribution. We concluded that a power-scaled model is reasonable with p-values > 0.05 for the normality tests, and the model had minimal variance and normally distributed residuals compared to the purely linear and log-transformed models.

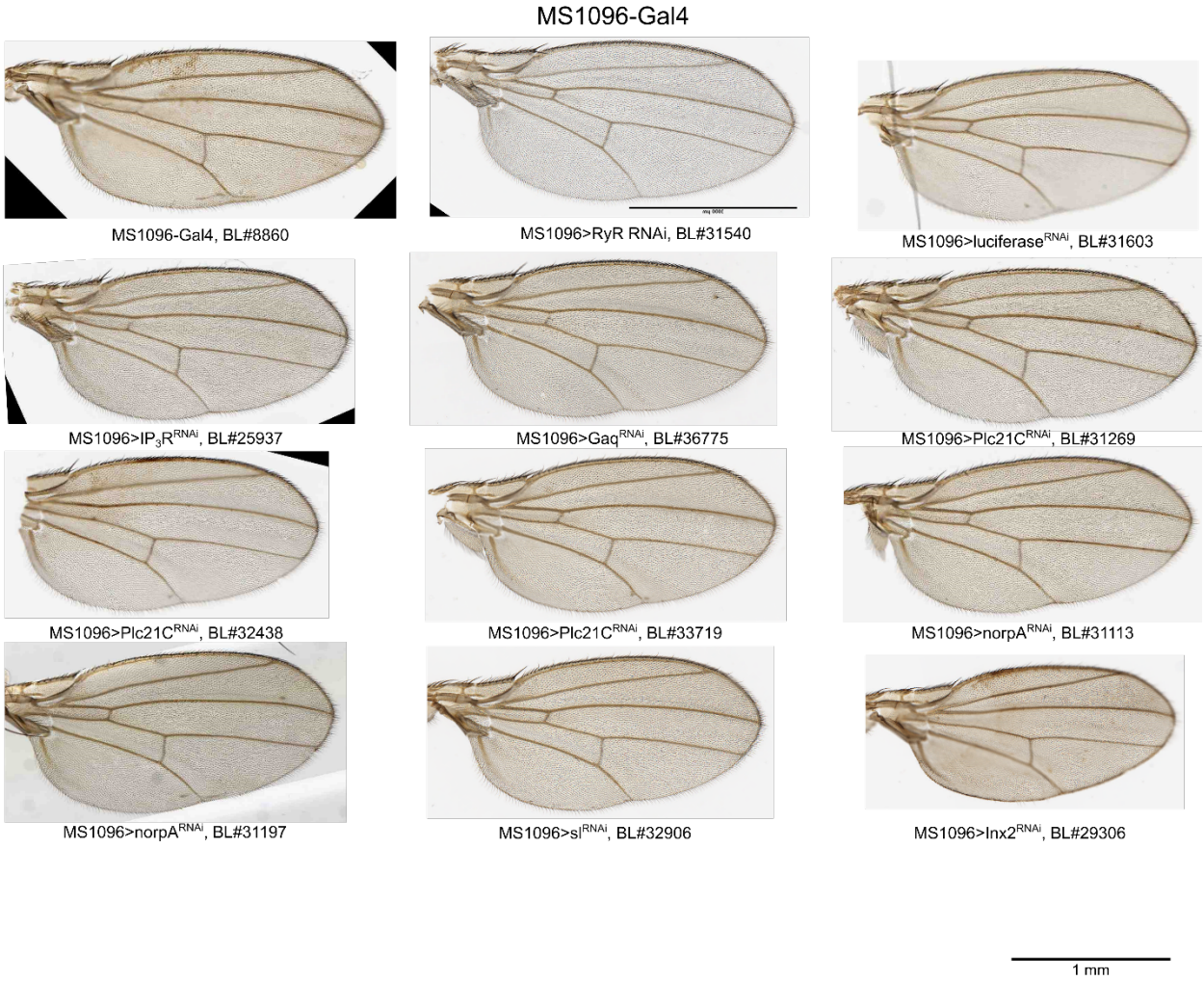

Figure S8: Representative wing phenotypes from the MS1096 crosses used in this study

The scale bar is 1 mm. For imaging the dorsal compartment specific MS1096-Gal4 driven crosses, the three-dimensional bending phenotype is obscured. Wing images were selected randomly from the sample of wings quantified in Fig. 2. The larval overgrowth phenotype generated by tkv^{CA} results in distorted wings.

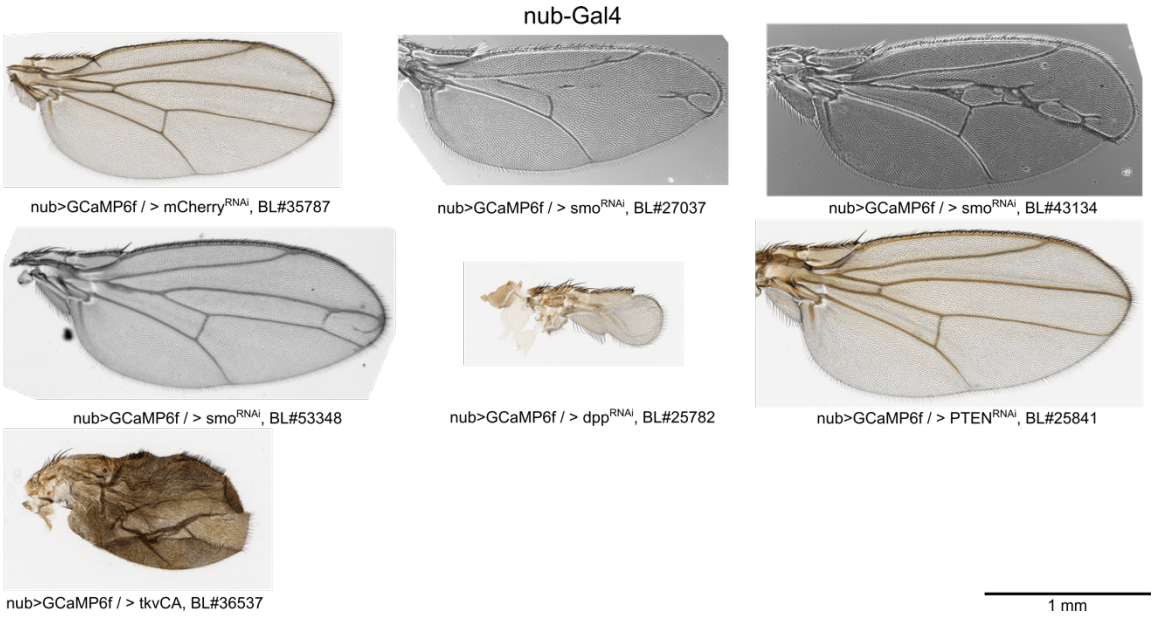

Figure S9: Representative wing phenotypes from the nub-GAL4>GCaMP6f crosses used in this study

The scale bar is 1 mm. To image Ca^{2+} dynamics in the wing disc pouch, we used nub-GAL4 to express genetically encoded Ca^{2+} sensor (GCaMP6f sensor). The larval overgrowth phenotype generated by tkv^{CA} results in distorted wings.

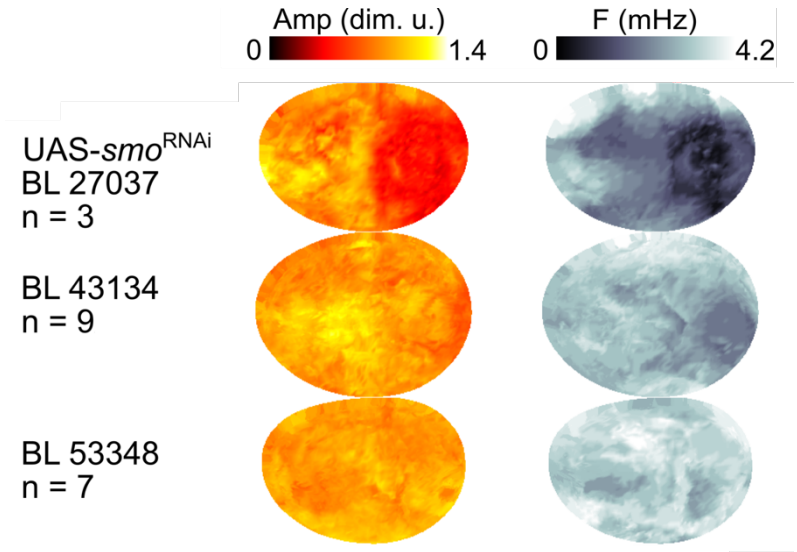

Figure S10: Multiple *Smo*^{RNAi} lines all abolish the anterior-posterior patterning of amplitude as shown in these composites.
For validation of RNAi knockdown strength refer to severity of wing phenotypes in Fig S9.

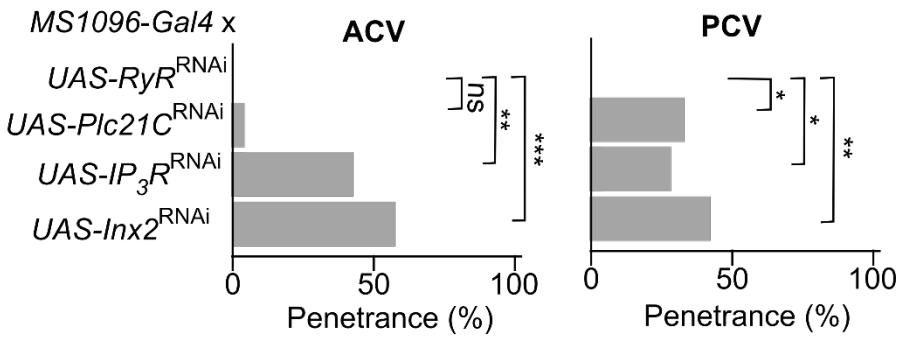

Figure S11: Quantification of anterior and posterior cross veins in various RNAi lines knockdowns.

ACV and PCV vein defects were observed when *RyR*, *Plc21C*, *IP3R* and *Inx2* genes were knocked down using *MS1096-GAL4* driver. ACV and PCV defects were quantified manually. Proportions test was performed, and the asterisks denote significance (* = $p < 0.05$, ** = $p < 0.01$, *** = $p < 0.001$, ns = not significant)

Table S1: Line validation details

Line	Condition	Validation
BL#25937	*UAS-IP3R^{RNAi}*	This RNAi line shows a documented wound healing phenotype described in (15), and epithelial folding defects described in (26)
BL#29306	*UAS-Inx2^{RNAi}*	This RNAi line shows a documented wound healing phenotype and phenocopies Ca^{2+} phenotype described in (15)
BL#42645	*UAS-Inx2^{RNAi}*	This RNAi line shows an auditory response phenotype documented in (93). This line shows qualitatively similar but weaker Ca^{2+} phenotypes compared to BL#29306
BL#27263	*UAS-SERCA^{RNAi}*	Wing phenotype in Fig. S8 matches SERCA^{RNAi} phenotypes of BL#24928 shown in supplementary Figure 5 of (15)
BL#25928	*UAS-SERCA^{RNAi}*	Wing phenotype in Fig. S8 matches SERCA^{RNAi} phenotypes of BL#24928 shown in supplementary Figure 5 of (15)
BL#31540	*RyR^{RNAi}*	The lack of a phenotype in the wing or observed calcium signaling dynamics suggests that RyR plays an insignificant role in wing development. No expression of RyR has been reported in the wing disc (94).

Table S2: *Drosophila* lines

Name	Source	Genotype
nub-Gal4, UAS-GCaMP6f	(29)	nub-GAL4, UAS-GCaMP6f/CyO, UAS-Dcr-2
MS1096-Gal4	BL#8860	w[1118] P{w[+mW.hs]=GawB}Bx[MS1096]
UAS-*dpp*^{RNAi}	BL#25782	y[1] v[1]; P{y[+t7.7] v[+t1.8]=TRiP.JF01371}attP2
UAS-*pten*^{RNAi}	BL#25841	y[1] v[1]; P{y[+t7.7] v[+t1.8]=TRiP.JF01859}attP2
UAS-IP3R^{RNAi}	BL#25937	y[1] v[1]; P{y[+t7.7] v[+t1.8]=TRiP.JF01957}attP2
UAS-*Inx2*^{RNAi}	BL#29306	y[1] v[1]; P{y[+t7.7] v[+t1.8]=TRiP.JF02446}attP2
UAS-norpA^{RNAi}	BL#31113	y[1] v[1]; P{y[+t7.7] v[+t1.8]=TRiP.JF01585}attP2
UAS-norpA^{RNAi}	BL#31197	y[1] v[1]; P{y[+t7.7] v[+t1.8]=TRiP.JF01713}attP2
UAS-Plc21C^{RNAi}	BL#31269	y[1] v[1]; P{y[+t7.7] v[+t1.8]=TRiP.JF01210}attP2
UAS-luciferace^{RNAi}	BL#31603	y[1] v[1]; P{y[+t7.7] v[+t1.8]=TRiP.JF01355}attP2
UAS-Plc21C^{RNAi}	BL#32438	y[1] sc[*] v[1]; P{y[+t7.7] v[+t1.8]=TRiP.HMS00436}attP2/TM3, Sb[1]
UAS-*sf*^{RNAi}	BL#32906	y[1] sc[*] v[1]; P{y[+t7.7] v[+t1.8]=TRiP.HMS00695}attP2
UAS-*dpp*^{RNAi}	BL#33618	y[1] v[1]; P{y[+t7.7] v[+t1.8]=TRiP.HMS00011}attP2
UAS-Plc21C^{RNAi}	BL#33719	y[1] sc[*] v[1]; P{y[+t7.7] v[+t1.8]=TRiP.HMS00600}attP2
UAS-tkv^{CA}	BL#36537	w[*]; P{w[+mC]=UAS-tkv.CA}3
UAS-Gaq^{RNAi}	BL#36775	y[1] v[1]; P{y[+t7.7] v[+t1.8]=TRiP.JF02390}attP2
UAS-*smo*^{RNAi}	BL#27037	y[1] v[1]; P{y[+t7.7] v[+t1.8]=TRiP.JF02363}attP2
UAS-*smo*^{RNAi}	BL#43134	y[1] v[1]; P{y[+t7.7] v[+t1.8]=TRiP.GL01472}attP2
UAS-*smo*^{RNAi}	BL#53348	y[1] sc[*] v[1]; P{y[+t7.7] v[+t1.8]=TRiP.HMC03577}attP40
UAS-mCherry	BL#35787	y[1] sc[*] v[1]; P{y[+t7.7] v[+t1.8]=UAS-mCherry.VALIUM10}attP2
UAS-*SERCA*^{RNAi}	BL#44581	y[1] sc[*] v[1]; P{y[+t7.7] v[+t1.8]=TRiP.HMS02878}attP2

Table S3: MS1096-Gal4>UAS-RNAi phenotype summary

Gene	Function	Phenotype
IP_3R	Releases Ca^{2+} from ER to cytosol	Bent wings, smaller, increases vein differentiation defects
Gαq	Produces PLCβ	Bent wings, smaller, vein differentiation
Inx2	Forms gap junctions	Bent wings, smaller, vein differentiation
SERCA	Pumps Ca^{2+} from cytosol to ER	Shriveled wings (strong)
norpA	PLCβ4 homolog, produces IP_3	Normal
Plc21C	PLCβ1 homolog, produces IP_3	Bent wings, vein differentiation defects
sl	PLCγ homolog, produces IP_3	Bent wings, smaller, vein differentiation

Table S4: Parameters of feature extraction pipeline

Parameter	Optimized Value	Meaning
Amp_{min}	0.29	Minimum peak amplitude
WHM_{min}	23 s	Minimum duration of peak
Refractory Period	10 s	Minimum time between peaks
σ_{min}	8 s	Parameter for high-frequency Gaussian filter for removing noise
σ_{max}	1100 s	Parameter for low-frequency Gaussian filter for adapting to changes in basal level

Table S5: Extended data movies

SI Movie #	Description
1	nub-Gal4>UAS-GCaMP6f, in vivo, spike
2	nub-Gal4>UAS-GCaMP6f, in vivo, ICT
3	nub-Gal4>UAS-GCaMP6f, in vivo, ICW
4	nub-Gal4>UAS-GCaMP6f, in vivo, fluttering
5	nub-G4>UAS-GCaMP6f/ UAS-IP_3R^{RNAi}, in vivo, BL# 25937
6	nub-G4>UAS-GCaMP6f/UAS-$SERCA^{RNAi}$, in vivo, BL# 44581
7	nub-G4>UAS-GCaMP6f/UAS-$Inx2^{RNAi}$, in vivo, BL# 29306
8	nub-G4>UAS-GCaMP6f/UAS-$Plc21C^{RNAi}$, in vivo, BL# 31269
9	nub-G4>UAS-GCaMP6f/UAS-$norpA^{RNAi}$, in vivo, BL# 31113
10	nub-G4>UAS-GCaMP6f/UAS-sl^{RNAi}, in vivo, BL# 32906
11	nub-G4>UAS-GCaMP6f/UAS-$G\alpha q^{RNAi}$, ex vivo, BL# 36775
12	nub-G4>UAS-GCaMP6f/UAS-IP_3R^{RNAi}, ex vivo, BL# 25937
13	nub-G4>UAS-GCaMP6f/UAS-$Plc21C^{RNAi}$, ex vivo, BL# 31269
14	nub-Gal4>UAS-GCaMP6f, in ZB media + 0% FEX
15	nub-Gal4>UAS-GCaMP6f, in ZB media + 2.5% FEX
16	nub-Gal4>UAS-GCaMP6f, in ZB media + 5% FEX
17	nub-Gal4>UAS-GCaMP6f, in ZB media + 10% FEX
18	nub-Gal4>UAS-GCaMP6f, in ZB media + 20% FEX
19	nub-Gal4>UAS-GCaMP6f, in ZB media + 40% FEX
20	nub-G4>UAS-GCaMP6f/UAS-$Inx2^{RNAi}$, ex vivo, BL# 29306
21	nub-G4>UAS-GCaMP6f/UAS-Smo^{RNAi}, ex vivo, BL# 43134
22	nub-G4>UAS-GCaMP6f/UAS-Dpp^{RNAi}, ex vivo, BL# 25782
23	nub-G4>UAS-GCaMP6f/UAS-$Pten^{RNAi}$, ex vivo, BL# 25841
24	nub-G4>UAS-GCaMP6f/UAS-mCherry, ex vivo, BL# 35787

FEX: fly extract

Table S6: Qualitative proportion p-values

Calculated categorical proportions for each tested knockdown are shown below. The proportion of each type of activity was compared with unperturbed *nub-Gal4>UAS-GCaMP6f* wandering larvae. We report p-values obtained from the proportion test. p-values under 0.05 are highlighted and considered significant. For example, all conditions show a difference in total activity except for *norpA*^{RNAi} and *sl*^{RNAi}; however, the *sl*^{RNAi} condition spends proportionally more time undergoing spike activity and less time undergoing waves and fluttering than the unperturbed control. Raw measurements are reported in Table S6. Bold highlights indicate significant differences (p-value < 0.05).

IP$_3$R^{RNAi}	**3.0E-03**	9.7E-01	4.2E-01	**2.6E-02**	**3.1E-02**
SERCA^{RNAi}	**9.5E-06**	3.3E-01	**2.8E-02**	**4.3E-03**	**3.9E-02**
Inx2^{RNAi}	**8.1E-50**	**3.2E-99**	4.0E-01	2.6E-01	5.3E-02
Gαq^{RNAi}	**1.3E-06**	3.1E-01	**6.7E-03**	**3.2E-03**	**3.3E-02**
Plc21C^{RNAi}	**9.3E-06**	3.8E-01	**6.5E-03**	**5.8E-03**	**7.3E-03**
norpA^{RNAi}	8.3E-01	8.9E-01	**9.5E-03**	1.5E-01	**2.2E-02**
sl^{RNAi}	4.7E-01	**5.3E-05**	**3.3E-03**	**7.8E-03**	**1.5E-02**
smo^{RNAi}	**4.5E-04**	9.7E-02	6.1E-01	**8.7E-07**	**3.8E-02**

Table S7: Qualitative proportion raw values for in vivo data

Control	0.87	0.01	0.04	0.05	0.03	790	103
IP$_3$R^{RNAi}	0.95	0.01	0.03	0.01	0.00	164	19
SERCA^{RNAi}	0.99	0.00	0.01	0.00	0.00	150	21
Inx2^{RNAi}	0.30	0.56	0.06	0.08	0.00	131	16
Gαq^{RNAi}	1.00	0.00	0.00	0.00	0.00	54	6
Plc21C^{RNAi}	0.97	0.01	0.01	0.01	0.00	253	36
norpA^{RNAi}	0.88	0.01	0.09	0.03	0.00	185	22
sl^{RNAi}	0.85	0.04	0.10	0.01	0.00	207	25
smo^{RNAi}	0.78	0.02	0.05	0.14	0.01	290	40

Control is the average of multiple days (day 5-8). Due to smaller available sample sizes, genetic perturbations are within a three-day egg laying window.